



POLITECNICO
MILANO 1863

SCUOLA DI INGEGNERIA INDUSTRIALE
E DELL'INFORMAZIONE

DNS of a Turbulent Channel Flow with Partial Slip

TESI DI LAUREA MAGISTRALE IN
AERONAUTICAL ENGINEERING - INGEGNERIA AERONAUTICA

Author: **Aditya Raman**

Student ID: 964455

Advisor: Prof. Maurizio Quadrio

Academic Year: 2022-23

Abstract

A turbulent flow in a channel is analysed with a primary objective to reduce the skin friction drag using spatial modulation of partial slip. This spatial modulation is expected to produce spanwise forcing and suppress turbulence similar to the active control methods such as the oscillating wall techniques and travelling waves, while overcoming the energy challenges associated with active control. However, the lack of exposure in such partial slip cases requires one to delve into cases with abundant literature that can shed light on the drag reduction phenomenon. The study aims to do that using slip conditions. In order to simulate the flow, Direct Numerical Simulations (DNS) with a pseudo-spectral approach has been employed. Simulations have been carried out with data similar to relevant literature for an accurate comparison. Furthermore, slip cases are compared with the no slip counterpart to quantify drag reduction and characterize statistics. To ensure the accuracy, the no slip reference cases are validated with the relevant literature. It is observed that the presence of streamwise slip conditions create low Reynolds number effects, and reduces the skin-friction drag. The reduction in drag is corroborated by a two fold procedure. Furthermore, the introduction of slip velocity is observed to modify the turbulence dynamics particularly, by lowering the production activity near the wall. Although the general behaviour of statistics is coherent with the knowledge of turbulent channel flow, some specific deviating trends signal the need to increase the sample size. Some insights are provided on modifying the geometry further to attain spanwise forcing and possibly drag reduction.

Keywords: partial slip, turbulence, drag reduction, pseudo-spectral

Contents

Abstract	i
Contents	ii
1 Introduction	1
2 Methodology	4
2.1 Pseudo-spectral approach	4
2.2 Computational Domain	6
2.3 Numerical method	7
2.3.1 Spatial discretization	7
2.3.2 Temporal Discretization	9
2.3.3 Solution Procedure	10
2.4 Code Structure	10
2.5 Slip boundary	11
2.6 Numerical parameters	13
3 Results	15
3.1 Drag Reduction	15
3.2 Drag Reduction: A theoretical prediction	16
3.3 Statistical Notations	17
3.4 Mean Properties	18
3.5 Law of the wall	21
3.5.1 ΔB : A theoretical comparison	22
3.6 Turbulent Intensities	23
3.7 Shear Stresses	25
3.8 Turbulent Kinetic Energy	29
4 Conclusions and Future developments	34

Bibliography	36
List of Figures	39
Acknowledgements	40
Abstract in Italian	41

1 | Introduction

Friction drag is an essential component of the total drag in a turbulent regime, that restricts the attainable efficiency and performance. For example, in the aviation industry, it has been shown that viscous drag could amount to as much as 50% of the total drag [12]. Motivated by the fact that even a small percentage of drag reduction could increase the profit margins by a drastic amount, it has been a key subject of interest in research for decades now. This comes under the domain of flow control, where a small configuration change is applied to retrieve some real engineering benefits such as drag reduction. The flow control strategies are further categorised into Active and Passive techniques, where the former requires injection of energy into the system. Although it produces desirable results, the energy injection brings a great amount of complexity and costs. Therefore, this work is based on passive strategies, where a modification of geometry is performed without the energy input to obtain the desired results.

Among the passive concepts, the use of riblets is one of the most widespread, which was bio-inspired from the narrow grooves present on shark's scales and were employed in the walls to reduce drag [29] [28]. It has been shown that when longitudinal grooves are aligned with streamwise direction, it has the potential to reduce the turbulent friction drag[5]. In riblets, the drag reduction characteristics can be described with respect to the difference in protrusion heights between streamwise and spanwise directions [19] [1]. The protrusion height is defined as the distance between rib tips and average origin of the velocity profile near the surface, which essentially can be seen as a slip length [26]. It was shown by Garcia-Mayoral & Jiminez [10] [9] that presence of streamwise slip at the plane of riblet tips itself can lead to drag reduction; by increasing the streamwise velocity. This is where super hydrophobic surfaces come into play, which were again bio-inspired by water-repellent properties of lotus leaves, with a very large contact angles. Superhydrophobic surfaces have been a subject of research in fluid dynamics due to their very high contact angle and their potential to reduce drag [4]. To achieve a slip effect, micro or nano structured cavities can be fabricated on the structure, where small gas bubbles are trapped inside the cavities and therefore the liquid flow experiences negligible shear stress effectively reducing the skin-friction drag [27]. Despite their high capabilities, superhydrophobic

surfaces and drag reduction have not been yet used for practical applications, because the high pressure and high shear rate of turbulent flows in real world environments collapses the air pockets in the surface micro-texture [26] [3]. Therefore, a successful implementation of superhydrophobic surfaces in practical applications requires a detailed study on micro-textured surfaces and the drag reduction mechanism.

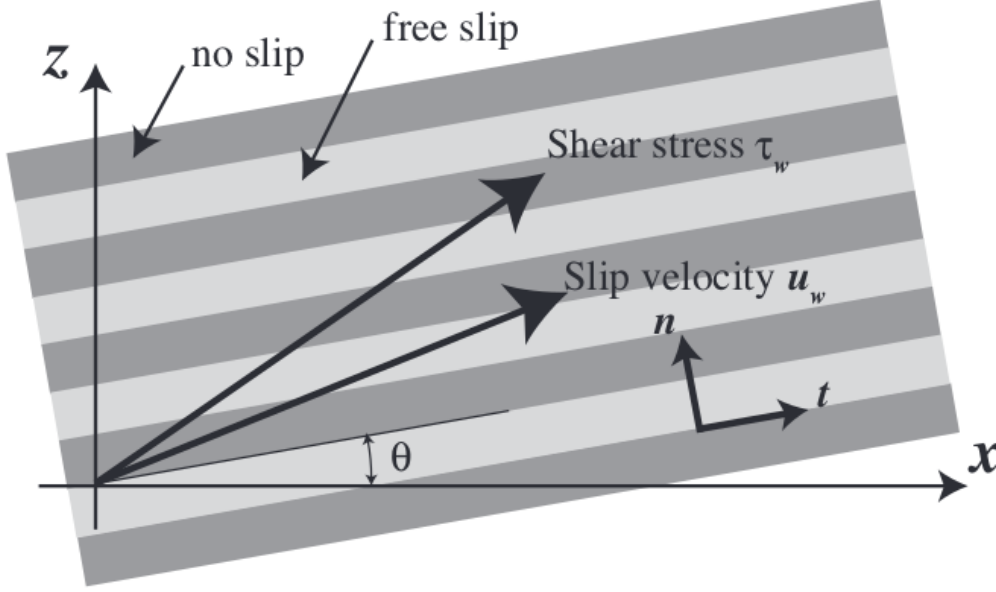


Figure 1.1: Sketch of a channel wall with alternating boundary conditions and inclined by an angle θ with respect to the streamwise direction [13]. x and z denote streamwise and spanwise directions respectively

In the field of active control, investigations into spanwise forcing methods such as the oscillating wall technique [14] and travelling waves [25] have proved in drag reduction by providing spanwise oscillations which further suppresses near wall turbulence. The primary objective of this study is to reproduce the mentioned spanwise forcing techniques using passive control strategy to overcome the energy consumption drawback. Various literature [22] [2] [8] have consistently shown that slip in streamwise direction brings in drag reduction and slip in spanwise direction causes drag increase. Consequently, there is a need to examine cases involving alternating slip and no slip boundary conditions [21] for the stated purpose. The primary objective in this study is to model the channel wall as a series of slip and no slip boundary conditions and to incline this partial slip system with respect to the freestream direction as shown in Fig.1.1 [13]. This is further expected to reproduce the aforementioned spanwise forcing method of the active control due to the introduction of spanwise slip velocity.

To proceed further, lack of exposure with partial slip cases makes it imperative to begin with cases that have abundant literature. In other words, a thorough examination of the code with homogeneous slip boundary conditions is an essential prerequisite to understand the mechanisms of drag reduction, accurately capture the statistics before proceeding further and testing for the primary objective. This crucial step that lays a solid foundation is exactly what this work intends to do.

This report is structured as follows: the methodology of the study is presented in §2 which gives information about the governing equations, domain, numerical method and the imposition of slip boundary condition. The results are categorized into drag reduction and various statistics characterization which are presented in §3. Finally in §4, some discussion about the results are presented along with some suggestions on a possible methodology for future developments.

2 | Methodology

This chapter contains details of the methodology employed such as the governing equations, numerical methods, solution procedure, computational domain, a brief description of the code employed from [20] and finally an explanation on how the slip boundary conditions can be modelled and imposed in the existing code.

2.1. Pseudo-spectral approach

The flow in the channel flow operates under the assumptions of unsteadiness, viscous and incompressibility. Therefore, the system of equations used to solve is non-dimensional Navier Stokes equations for an incompressible flow presented as follows:

$$\frac{\partial u}{\partial x} + \frac{\partial v}{\partial y} + \frac{\partial w}{\partial z} = 0 \quad (2.1)$$

$$\frac{\partial u}{\partial t} + u \frac{\partial u}{\partial x} + v \frac{\partial u}{\partial y} + w \frac{\partial u}{\partial z} = -\frac{\partial p}{\partial x} + \frac{1}{\text{Re}} \nabla^2 u \quad (2.2)$$

$$\frac{\partial v}{\partial t} + u \frac{\partial v}{\partial x} + v \frac{\partial v}{\partial y} + w \frac{\partial v}{\partial z} = -\frac{\partial p}{\partial y} + \frac{1}{\text{Re}} \nabla^2 v \quad (2.3)$$

$$\frac{\partial w}{\partial t} + u \frac{\partial w}{\partial x} + v \frac{\partial w}{\partial y} + w \frac{\partial w}{\partial z} = -\frac{\partial p}{\partial z} + \frac{1}{\text{Re}} \nabla^2 w \quad (2.4)$$

In order to close the equations, appropriate boundary conditions and initial conditions have to be imposed for all the variables. The usual approach is to use the periodic boundary condition in streamwise and spanwise directions. This effectively means that the equations can now be Fourier transformed along these directions due to the periodicity. This is at the base of a pseudo spectral approach which has been employed in this work. Essentially, the solver solves a different formulation of the non-dimensional incompressible Navier-Stokes mentioned above. This new formulation resembles the Orr-Sommerfeld stability equations but with a key distinction of being non-linear. An efficient such formulation of the system of equations was proposed by Kim, Moin and Moser documented in [15] in 1987. It involves an effective rearrangement of the system of equations to obtain significant

benefits. Essentially, the continuity and momentum equations are replaced by two other equations. The first one is a fourth order equation for wall normal velocity component as represented in eq. (2.6) and the second one for wall normal vorticity component as in eq. (2.6). As mentioned earlier, periodic boundary conditions essentially implies that this system can be coupled with fourier exapansions in wall parallel homogenous directions x and z . When such expansions are adopted, two fundamental advantages arise. The first one is that the pressure disappers from the equations reducing the complexity. The second advantage is that the wall parallel homogeneous velocity components can now be computed as a 2×2 algebraic system in this new framework as seen in eq. (2.7), making the approach highly computationally efficient [20].

$$\frac{\partial \hat{\eta}}{\partial t} = \frac{1}{\text{Re}} (D_2(\hat{\eta}) - k^2 \hat{\eta}) + i\beta \widehat{HU} - i\alpha \widehat{HW} \quad (2.5)$$

$$\frac{\partial}{\partial t} (D_2(\hat{v}) - k^2 \hat{v}) = \frac{1}{\text{Re}} (D_4(\hat{v}) - 2k^2 D_2(\hat{v}) + k^4 \hat{v}) - k^2 \widehat{HV} - D_1(i\alpha \widehat{HU} + i\beta \widehat{HW}) \quad (2.6)$$

$$\begin{cases} \hat{u} = \frac{1}{k^2} (i\alpha D_1(\hat{v}) - i\beta \hat{\eta}) \\ \hat{w} = \frac{1}{k^2} (i\alpha \hat{\eta} + i\beta D_1(\hat{v})) \end{cases} \quad (2.7)$$

where D_j stands for j^{th} derivative in the wall normal direction. α and β are the streamwise and spanwise wave numbers, with i being the imaginary unit. $k^2 = \alpha^2 + \beta^2$. The non linear terms on the other hand are embedded inside the following definitions:

$$\widehat{HU} = i\alpha \widehat{uw} + D_1(\widehat{uw}) + i\beta \widehat{uw} \quad (2.8)$$

$$\widehat{HV} = i\alpha \widehat{vw} + D_1(\widehat{vw}) + i\beta \widehat{vw} \quad (2.9)$$

$$\widehat{HW} = i\alpha \widehat{vw} + D_1(\widehat{vw}) + i\beta \widehat{vw} \quad (2.10)$$

Concerning the boundary conditons, the eq. (2.6) being a fourth ordered requires imposition of four boundary conditions- two for each wall. The no penetration boundary condition is a requisite for two walls translating as $\hat{v}=0$ at y_u and y_l . Another boundary condition is a direct consequence of the continuity equation at two walls translating as $D_1(\hat{v})=0$ closing the mentioned equation. The eq. (2.5) on the other hand is a second ordered therefore requiring one boundary condition for each wall. The conventional no slip boundary condition in this framework is $\hat{\eta}=0$ on both the walls. Regarding the slip conditon, it is presented in Sec.2.5. Other than the boundary conditions, initial conditions have to be imposed for \hat{v} . The initial condition for $\hat{\eta}$ on the other hand can be directly

computed from \hat{v} and then be imposed.

The forcing terms are needed to force the fluid across the channel. This forcing term could be an imposed pressure gradient resulting in the approach of Constant Pressure Gradient (CPG). Another choice could be to choose the time dependent spatially uniform pressure gradient in such a way that the flow rate remains constant resulting an approach called Constant Flow Rate (CFR). In this study, the CFR approach has been used.

2.2. Computational Domain

One of the most important flows that aids in understanding the principles of fluid dynamics is the plane channel flow. The flow is characterized by viscous motion of fluid between two parallel plates that extend indefinitely in streamwise and spanwise directions. This simplified configuration has been proved as a representative model to understand various fundamentals of fluid dynamics including turbulence. In this configuration, the motion of the fluid is along the streamwise direction while varying in the wall normal direction. The streamwise and spanwise directions on the other hand are periodic making the system statistically one dimensional.

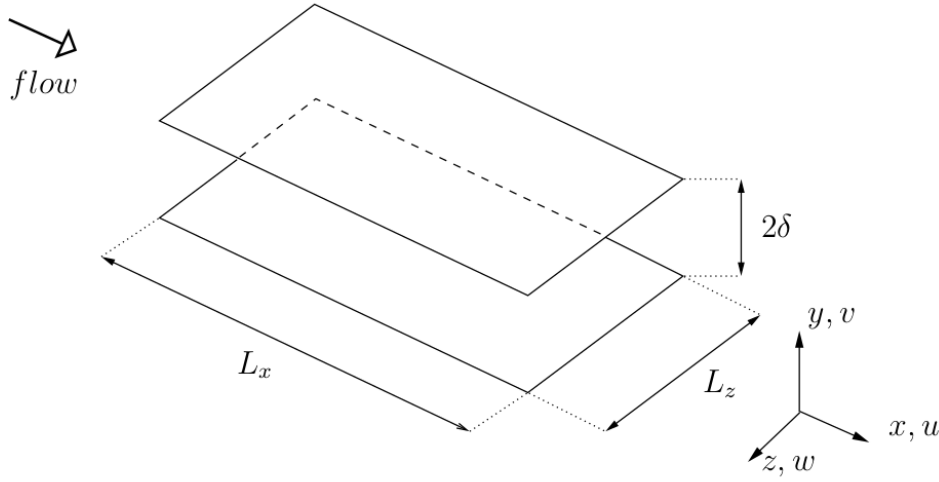


Figure 2.1: Computational domain [20]

The computational domain illustrated in Fig.2.1 [20], is a sketch of a plane channel flow. A cartesian coordinate system is employed in this study where the streamwise, wall-normal and spanwise directions are represented by x, y, z respectively. In the spatial domain, the velocity vector components in the respective directions are denoted by u, v, w . Due to the periodic and statistically one dimensional nature, a significant advantage arises

in characterizing the reference length scale as now it is along a single direction namely wall-normal. Consequently, the reference length is denoted as δ , which is defined as one half the height of a channel as in eq.(2.11), where the channel height is 2δ .

$$\delta = \frac{y_u - y_l}{2} \quad (2.11)$$

where y_u denotes the wall normal position of upper wall and y_l denotes the wall normal position of lower wall.

In this study, the size of the domain was selected the same as used by Min&Kim [22] so that results can be compared more accurately. Therefore, the lengths in directions x, y, z which are denoted as L_x, L_y, L_z are of the size $7\delta \times 2\delta \times 3.5\delta$ in streamwise, wall normal and spanwise directions respectively. Another crucial parameter is the Reynolds number, which can be defined as in eq. (2.12) using δ as the characteristic length.

$$Re = \frac{U\delta}{\nu} \quad (2.12)$$

where ν is the kinematic viscosity of the fluid. In this work, the Reynolds number is defined by choosing the centerline velocity as the reference velocity, which makes it a centerline Reynolds number denoted by Re_c .

2.3. Numerical method

In this section, the various numerical methods employed have been discussed. Specifically, three distinct numerical methods have been emphasized upon, the spatial methods used for homogeneous directions and for wall normal direction and the temporal method.

2.3.1. Spatial discretization

In Sec. 2.1, it has been clearly expressed the need for Fourier discretization in the homogeneous directions. Essentially it means to expand the unknown quantities by a truncated Fourier series. Once the directions are Fourier discretized, now the directions are described in terms of wave numbers as seen in Sec. 2.1 recalling that α and β being wavenumbers

for streamwise and spanwise direction respectively.

$$\alpha = \frac{2\pi ix}{L_x} = \alpha_0 ix \quad (2.13)$$

$$\beta = \frac{2\pi iz}{L_z} = \beta_0 iz \quad (2.14)$$

where ix and iz are the indices corresponding to streamwise and spanwise directions respectively, such that ix goes from $-nx$ to $+nx$ and iz goes from $-nz$ to $+nz$. nx and nz are half the number of Fourier modes in streamwise and spanwise directions respectively. α_0 and β_0 are the two fundamental wave number parameters that basically describes the size of the domain in homogeneous directions as $L_x = 2\pi/\alpha_0$ and $L_z = 2\pi/\beta_0$.

Another aspect with Fourier modes is that the non linear terms appear as convolutions in Fourier space. Although the Fourier expansions trumps in the context of computational costs, the convolutions increases the cost. In order to resolve this issue, the three Fourier components are inverse transformed to physical space, all possible combinations of velocity products are computed and then forth transformed to Fourier space effectively saving the efficiency. In order to transform often from Fourier space to physical space vice-versa, Fast Fourier Transform (FFT) algorithm has been employed.

With using FFT in a pseudo-spectral environment, there is always a risk of encountering a very specific error called the 'Aliasing error'. Aliasing errors essentially occur when the size of sampled Fourier modes is less than the actual size of Fourier modes leading to a spectral leakage. In essence, the modes that are out of range is aliased to a mode with wavenumber inside the domain. This leads to additional peaks in the frequency domain which further leads to inaccurate analysis. With such a pseudo-spectral code, the process of convolutions is specifically vulnerable to aliasing errors as the wavenumbers there exceeds the range. In the code used in this work, this aliasing errors is removed by first expanding the modes by a factor of 3/2 before the inverse transformation. Then zero padding is done in the expanded modes as in the expanded modes have been initialised a value of zero, and finally inverse transform is performed. This way the spurious energy from the high frequency modes into the low frequency modes are discarded.

The equations in Sec.2.1 shows the presence of D_j derivatives in wall normal direction. These derivatives are discretized with compact finite difference schemes. In contrast to the conventional finite difference schemes, the compact finite difference methods provide a better representation of shorter length scales essentially bringing them closer to spectral resolution [16] while retaining the liberty in adapting mesh geometry and boundary conditions. The difference in compact schemes and regular finite difference schemes lies in the

accuracy of the compact schemes at every grid point. This accuracy is attained by replacing the interpolation polynomial of regular schemes in frequency space into a ratio of two polynomials. Consequently, this feature is advantageous when dealing with polynomial behaviours in Fourier space, giving it a spectral like resolution [16]. Specifically, pentadiagonal schemes have been implemented in the code, where the exact derivative operator D_j at a point y_i in the wall normal direction is discretized by five coefficients $d_j(i)$ at five wall normal points centered at y_i , therefore from y_{i-2} to y_{i+2} making it a centered scheme with fourth order accuracy [20]. Although, when it comes to the boundaries, non-centered schemes are used to compute properly the derivatives. A ghost node strategy is employed beyond the walls. In essence, the usage of such schemes in the wall normal direction coupled with Fourier in wall parallel directions makes the approach pseudo-spectral.

Since turbulent flows often display varying characteristics in different spatial directions, the anisotropy necessitates the need for variable size meshing in the wall normal direction. Variable meshing proves to be an optimal compromise in terms of computational efficiency and capturing flow behaviour more accurately. The usage of variable meshing means to use a finer or coarse meshing depending on the requirement at that spatial position. In order to fulfill the requirement, a hyperbolic tangent law is adopted in the wall normal discretization discarding the conventional uniform meshing. Therefore, this hyperbolic tangent law offers means to refine the mesh especially in the near wall region, where turbulent intensities are high due to wall effects. Where in the uniform meshing, the meshing is solely dependent on the discrete points and wall normal distance, with the hyperbolic tangent law, it is now dependent on tanh of a coefficient denoted as `htcoeff` in this code, which dictates how the mesh can be adapted in different wall normal positions.

2.3.2. Temporal Discretization

Concerning the temporal integration of the eqs.(2.5) and (2.6), a partially implicit method has been adopted in the code [20] [15] which essentially results in lower memory consumption. Specifically, the equations are categorized in to two sets to impose the time advancement schemes. The explicit part of the equations which can benefit highly from the higher-accuracy schemes, are integrated with the explicit time schemes. The drawbacks of explicit schemes include a very strong stability constraint which makes the choice of time step Δt to be very low and in accordance with the absolute stability leading to a large computational time. This drawback is intelligently managed when the stability limiting viscous part of the equations are subjected to implicit time advancement schemes. This way, the strong stability constraint on Δt is relieved for a part of the equations making it computationally cheaper. In this code, integration of explicit part of the equations

are performed by explicit third-order Runge-Kutta method. The viscous part on the other hand is subjected to an implicit second-order Crank-Nicholson scheme.

2.3.3. Solution Procedure

The way to solve the discretized equations can be illustrated in various steps [20]. The first step corresponds to assembling the right hand side of explicitly integrated parts of the equation. At a fixed time, with the knowledge of Fourier coefficients of the velocity at different wall normal positions, velocity products and their spatial derivatives can be computed. Then, the spatial derivatives are assembled with the right hand side values at previous time. The next step involves in solving the system. For a pair of streamwise and spanwise wave numbers, the finite difference discretization results in two pentadiagonal matrices from which \hat{v} and $\hat{\eta}$ can be computed. Once they are known, the wall parallel velocity components \hat{u} and \hat{w} can be computed from eq.(2.7).

2.4. Code Structure

The methodology of Pseudo-spectral discretized equations are simulated using Direct Numerical Simulations (DNS) in CPL [18], which is a general purpose programming language similar to FORTRAN or C with some unique features such as pointers flexibility conceived by Prof. Paolo Luchini. In this work a code using the stated approach is used, and the brief structure of which is described in this section. The overall code is segregated into five different files which are listed below.

- channel.cpl
- dnsdata.cpl
- dnsdirect.cpl
- rbmatmod.cpl
- dns.in

The file channel.cpl is the main file of the code which contains a main loop over time steps. At a given time, the rest of the procedure is performed. The file dns.in contains various input parameters such as resolution, time step size, total integration time etc. The file rbmatmod.cpl takes care of the matrix algebra such as LU decomposition. The rest of the files dnsdata.cpl and dnsdirect.cpl contains the various numerical strategies described in Sec. 2.3. The wall normal discretization using the hyperbolic tangent law is used in the file dnsdata.cpl. The module setup_derivatives in dnsdata.cpl is responsible for

computing the finite difference coefficients for the inner points. `dnsdata.cpl` also handles the operations of input/output and reading/writing data. Velocity is made by a structure of three complex numbers for three components and denoted in the code as `'V(0..nx,-nz..nz,-1..ny+1)'`, where the range exhibit the modes in streamwise, spanwise and wall-normal direction respectively. Only half the Fourier modes in streamwise direction are actually stored due to Hermitian symmetry [20]. For the wall normal direction, -1 and `ny+1` denote the ghost nodes below and above the wall respectively with `'iy=0'` being lower wall and `'iy=ny'` being the upper wall.

Three important subroutines are present in `dnsdirect.cpl` namely `convolutions`, `buildrhs` and `linsolve`. These subroutines perform major part of the job described in Sec.2.3.3. The subroutine `convolutions` is responsible for performing the inverse transform, computing velocity products and forth transforming as illustrated in sec. 2.3.1. The subroutine `buildrhs` is the main routine that uses the information from `convolutions` and builds the spatial derivatives and assembles the right hand side quantities of the discretized equations. The important aspect here is that at this point inside the time loop, `V.u` stores the right hand side of the equation (2.5). The mean profile on the other hand is saved when k^2 described in sec. 2.1 is zero. Therefore in the discretized sense when `ix` and `iz` described in sec. 2.3.1 are equal to zero; essentially in `'V(0,0,*).u'`.

The subroutine `linsolve` on the other hand is the major routine involving in solving the built equations and gives the values of \hat{v} and $\hat{\eta}$. Once the two primitive variables are computed, the subroutine `vetaTOuvw` takes care of the transformation of the primitive variables to the components of velocity. The important aspect is that it is only at this point of the time loop, where the array `'V'` actually contains Fourier coefficients of velocity. Finally the time loop is completed when flow rate corrections are performed by subroutine `compute_flowrate`. The described methodology in overall is for interior points. The boundary conditions which are applied before the solution process by changing the boundary lines of the matrices, are taken care by subroutine `applybc_0` and `applybc_n`. There is also a provision of structures `bc0` and `bcn` which stores the imposed boundary condition. This is especially advantageous in this work, where the slip boundary conditions had to be imposed and the array `'V.u'` stores the right hand side of equation creating a complexity with the imposition.

2.5. Slip boundary

In the context of fluid flows over a wall, two commonly imposed boundary conditions are the 'No slip' and 'No penetration' conditions. The no penetration condition implies

that the fluid is unable to permeate through the solid boundary. Mathematically, this means that the wall normal component of fluid velocity is zero which represents an exact boundary condition from a physical standpoint. On the contrary, the no slip condition has been conventionally accepted for most of the macroscopic flows. However, this assumption can be questioned when dealing with the analysis of micro or nano scales. At such low scales, the no slip conditions can be questioned due to the influence of wetting ability of the fluid on the momentum exchange ability with the surface at the atomic level [4]. This results in a slip velocity of the fluid at the solid wall. Consequently, in scenarios where the superhydrophobic surfaces featuring micro-textured cavities are used, a partial slip boundary condition becomes more appropriate.

The partial slip condition can be defined using the Navier slip condition. The Navier slip model is a Robin boundary condition eq.(2.15) which relates the velocity at the wall to the wall normal derivative at the wall through a proportionality constant called the slip length. The slip length represents the distance over which the fluid transitions from no-slip to the fluid velocity. In other words, it is the distance from the boundary where the linearly extrapolated fluid velocity vanishes. The slip length acts as a crucial parameter in defining the partial slip condition.

$$u_s|_w = \lambda \frac{du}{dy}|_w \quad (2.15)$$

where $u_s|_w$ is the streamwise slip velocity at the wall, λ is the slip length, $\frac{du}{dy}|_w$ denotes the shear rate.

The slip length λ in general depends on the shear rate $\frac{du}{dy}|_w$. Infact, it was proved to have a linear dependence on the shear rate [4]. But in cases where the shear rates are moderate, it can be assumed to be independent of the same [22] [23]. Min and Kim [22] studied the effects of slip length and drag reduction in turbulent flows and their work indicates that in order to have a noticeable drag reduction λ^+ i.e. when normalised by friction units has to be atleast 0.2. Consequently, in this study λ in global units was adopted as 0.02.

As explained in Sec.2.1, with the primitive variables as $\hat{\eta}$ and \hat{v} , the boundary conditions would have to be imposed for these variables instead of u . The no slip condition has a simple translation making $\hat{\eta}$ and \hat{v} zero at the walls. The slip conditions therefore have to be translated into primitive variables. This translation brings in a complexity from the nature of the code, where to improve the computational efficiency, the variable built for streamwise velocity is used in storing the right hand side of the eq.(2.5) as explained in Sec.2.4. The structure 'bc0' and 'bcn' introduced in Sec.2.4 were invoked to store the

values of the slip velocity at the beginning of the time loop and is conveniently used for handling the conversion to η well inside the loop. Referring to Sec.2.3.1, the non-centered schemes at the boundaries in combination with the ghost node approach was used to impose the slip velocity.

2.6. Numerical parameters

As explained in the previous sections, a pseudo-spectral DNS in CPL was employed to solve the problem at hand. This section reports the various numerical parameters that have been used concerning the operation of pseudo-spectral DNS. The first parameters that needs a description is the mesh resolution, which are Fourier modes in wall parallel planes. The resolution employed in this study $nx \times ny \times nz$ is $64 \times 100 \times 64$, where nx, ny, nz represents the modes in the streamwise, wall normal and spanwise directions respectively. Although the same number of Fourier modes are used in both the wall parallel directions, only half of the streamwise modes are actually stored owing to the Hermitian symmetry [20]. The ghost node strategy mentioned in Sec.2.3.1 essentially implies that the wall normal directions also contains the points '-1' and '101'. The coefficient for the hyperbolic tangent law in wall-normal meshing is of the value 1.5.

It has already been mentioned in Sec.2.2 that the Reynolds number used in the study is the one of the centerline. The value of the same is $Re_c=4200$ which corresponds to a friction Reynolds number $Re_{\tau_0}=\frac{u_{\tau_0}\delta}{\nu}=180$; where u_{τ_0} is the friction velocity of a conventional channel flow with no slip boundary conditions. As previously mentioned 2.3.1, in the Fourier directions, the domain size is now dictated by the two fundamental wave numbers α_0 and β_0 . The numerical values of the same are $\alpha_0=0.8976$ and $\beta_0=1.7952$. The size in the wall normal direction was taken to be 2 units. These values make the results more reliable as the the case study is now similar to the study of Min-Kim [22].

Concerning the initial field, it was generated from the same code with a resolution of $32 \times 100 \times 32$ with no-slip boundary conditions. Then, the spectral interpolation was used to reach the current resolution and domain which was integrated further in time to achieve a statistically steady state. The identification of this steady state was confirmed using total shear stress which has a linear profile and friction at the wall. Once the steady state was attained, the field was used as an initial field for further simulating two cases: the slip and the no-slip.

The time units employed are encoded in the definition of Reynolds number. As explained, the work employs a centerline Reynolds number Re_c and therefore the time units are defined in terms of U_c/δ . The analysis were carried out for maximum integration time of

500 units. The simulations were performed using CFL(Courant-Friedrichs-Lewy) number of 1.5. The task was performed on a personal computer equipped with 16 GB RAM, and each simulation required approximately 13 hours to complete. Snapshots across various times were captured and stored into the database, from which the statistics were computed and are discussed in the next sections.

3 | Results

3.1. Drag Reduction

Preliminary to the quantification of the statistics, a primary parameter that dictates the validity of the code is the percentage of drag reduction. This percentage was calculated in two different ways for the purpose of corroboration. First way involved monitoring the resulting mean pressure gradient as done by Min and Kim [22]. The expression is reported in equation (3.1)

$$DR = \frac{\left(-\frac{d\bar{p}}{dx}\right) - \left(-\frac{d\bar{p}}{dx}\right)_0}{-\frac{d\bar{p}}{dx}\big|_0} \times 100 \quad (3.1)$$

where DR represents percentage of drag reduction, $\frac{d\bar{p}}{dx}$ represents the mean pressure gradient and $\frac{d\bar{p}}{dx}\big|_0$ is the mean pressure gradient with respect to the conventional no-slip case.

The other way was to use the space-averaged friction which is a time dependent, spatially uniform wall normal derivative of streamwise mean velocity at the wall. This way, it essentially means to compute the skin-friction drag except for a dimensional factor of ν . Only the streamwise space averaged friction was used as the slip imposed was only along streamwise direction. The procedure involves computing the time average of space averaged friction for lower wall and taking an arithmetic average with respect to the upper wall to double the sample. Finally, the percentage is computed with respect to the reference no-slip case as done in equation (3.2)

$$DR = \frac{\frac{d\bar{u}}{dy} - \frac{d\bar{u}}{dy}\big|_0}{\frac{d\bar{u}}{dy}\big|_0} \times 100 \quad (3.2)$$

where $\frac{d\bar{u}}{dy}$ represents the double sampled space average friction of the slip case and $\frac{d\bar{u}}{dy}\big|_0$ denotes the same quantity for the no slip case.

The two different formulations yield nearly the same result. In table 3.1, the results are presented along with some other parameters as a comparison with respect to Min and Kim [22]. It can be clearly seen that it is well in accordance with the literature. The drag reduction percentage given in the table is using eq(3.2). The same quantity computed using eq(3.1) gives a value of -27.4% validating the numerical value even further.

Table 3.1: Comparison of study. + and * units describe normalisation with reference friction velocity u_{τ_0} and actual friction velocity u_{τ} respectively

Parameter	Min-Kim	Current Study
λ	0.02	0.02
λ^+	3.566	3.558
u_s^*	3.006	2.974
DR(%)	-29	-27.5

Despite matching many parameters with the relevant literature, there exists a minimal difference in the DR values. This can be attributed to the differences in wall normal resolution as the one used here is 100 in comparison to the value of 129 in the literature. The differences could also be due to the differences in numerical methods, as the literature uses second-order central difference to discretize all the spatial derivatives. Validating DR informs that the code is well performing and it is now important to characterize the statistics. Therefore in the next sections, various statistics are presented along with a no-slip case of $Re_{\tau_0}=180$ as done by Kim et.al 1987 [15].

3.2. Drag Reduction: A theoretical prediction

Fukagata et.al [8] proved in their work that it is possible to estimate the drag reduction theoretically for a turbulent flow in a channel with slip boundary conditions. Here the same prediction strategy is employed to compare with the results obtained in the Sec.3.1. The method employed in [8] essentially allows to calculate the drag reduction in slip case using the imposed constant slip length and reference friction velocity u_{τ_0} . The quantity drag reduction rate denotes as R_d can be defined as in eq.3.3.

$$R_d = \frac{C_{f_0} - C_f}{C_{f_0}} = 1 - \frac{u_{\tau}^2}{u_{\tau_0}^2} \quad (3.3)$$

where C_f and C_{f_0} denotes skin friction coefficient of slip and no slip case respectively.

Upon further mathematical operations, the eq.(3.3) can be expressed as follows:

$$u_{\tau}^{+} = \sqrt{1 - R_d} \quad (3.4)$$

where u_{τ}^{+} denotes the friction velocity of slip case in the wall units of no slip case.

When only the streamwise slip is considered, as done in this work, [8] proposes a relation between the slip length and the drag reduction rate through the eq.

$$\lambda^{+} = \frac{1 - u_{\tau}^{+}}{u_{\tau}^{+2}} (\kappa^{-1} \ln(Re_{\tau_0}) + F) - \frac{1}{\kappa u_{\tau}^{+}} \ln(u_{\tau}^{+}) \quad (3.5)$$

where κ is the von Karman constant and F is a constant from log-law version of Dean's formula [7]. $\kappa = 0.41$ and $F = 3.2$

In the eq.(3.5), for a given Re_{τ_0} and a slip length, the friction velocity of the slip case can be computed. Having known the friction velocity, it is possible to compute the drag reduction rate R_d from eq.(3.4). In the context of this work, the eq.(3.5) was used to theoretically estimate the drag reduction using the following value : $\lambda^{+} = 3.558$ from table 3.1. On imposing the values, the u_{τ}^{+} from eq.(3.5) was found to be of 0.86 which implies the unscaled friction velocity of slip case is 0.03 which fits perfectly with the value obtained in this study. Further, when the eq.(3.4) is used to compute the R_d , the obtained value shows up to be 0.267 implying a 26.7% drag reduction. This is in a very good agreement with the data obtained through the DNS of this study corroborating the validity of the work.

3.3. Statistical Notations

When analysing any statistics of turbulent flows, the velocity is analysed under Reynolds' decomposition where the velocity u is decomposed as $u = \bar{u} + u'$, where \bar{u} is the time averaged component and u' is the velocity component associated with the turbulent fluctuations. The Sec.3.4 deals with the description of the mean component \bar{u} and Sec.3.6 reports the statistics of fluctuating components u' . Since turbulence is a near wall phenomenon, it becomes necessary to non-dimensionalise the quantities with respect to friction units to magnify the effects near the wall. The conventional approach in the literature is to scale the quantities with friction velocity, but since in this study, friction velocities vary with respect to slip and no slip case, two key friction units have been introduced. Whenever a quantity is scaled with the actual friction velocity of each case i.e. u_{τ} , it is denoted

by * units and when the same is done with reference no slip friction velocity u_{τ_0} , it is described with + units. The flow is statistically symmetric about the mid-plane i.e. $y=\delta$ [24], therefore the statistics shown here are for lower half of the channel i.e. from $y=0$ the lower wall to $y=\delta$ the centerline. All the plots shown follow a common color code where red signifies quantification of the slip case and black implies no-slip case.

3.4. Mean Properties

In order to proceed and analyse the statistical differences in slip and no slip cases, it is imperative to determine the accuracy of the reference no slip case. This validation has been performed with the data of Kim et.al [15], where the same Re_{τ_0} has been employed. In table 3.2, some mean values of this study is reported along with the data of [15].

Table 3.2: Mean flow variables. τ_w is the shear stress at wall, c_f and C_f are skin friction coefficient obtained by centerline and bulk velocity respectively as defined in eqs.(3.6). u_b and u_c are the bulk and centerline velocities respectively.

Parameter	Kim et.al	Current Study
C_f	8.18×10^{-3}	7.96×10^{-3}
c_f	6.04×10^{-3}	5.98×10^{-3}
u_b/u_{τ_0}	15.63	15.85
u_c/u_{τ_0}	18.2	18.29

It is clear from the table 3.2 that the reference cases of this study can be considered reliable. The minimal differences are due to the small difference in the friction Reynolds number. Therefore, it is now safe to characterize and discuss the statistical differences between the two cases performed.

The mean profile is plotted in Fig.3.1 against the wall normal distance normalised by channel half height. The mean profile when plotted this way, the expected nature is to begin from a value depending upon the boundary conditions and reach the maximum value at the centerline. The preliminary observations include the lower resistance at the wall in slip case compared with the reference case, due to the introduction of slip velocity creating an offset at the wall, which makes the magnitude of the mean velocity at the wall to be $\bar{u} \approx 0.1$. The integral of the both the profiles across the channel half height confirms the constant flow rate approach followed. In the vicinity of the centerline, the reduction of mean velocity can be seen in the slip case with respect to the reference case

indicating a reduction of Reynolds number. This low Reynolds number effect can be seen better when plotted in $*$ units.

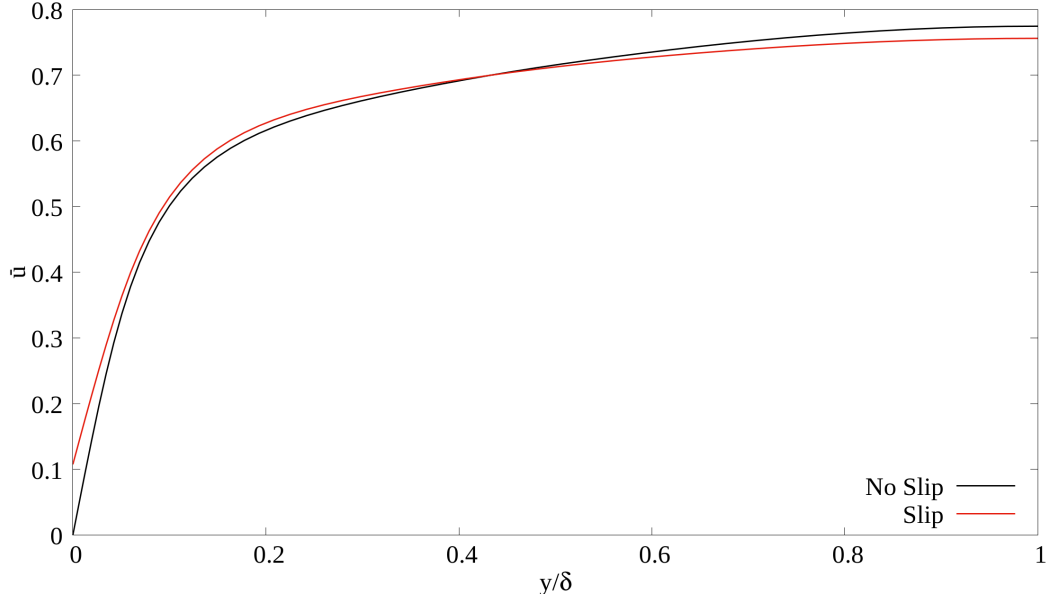


Figure 3.1: Mean Profile over channel half height in global units; \bar{u} :Mean Velocity

Therefore, in Fig.3.2, the mean streamwise velocity normalised with their actual friction velocities(u^*) have been plotted against the wall normal distance in friction units. In order to show the behaviour of friction normalised mean velocity across the channel, a log-lin format has been adopted in 3.2. Even though adopting such a scaling with a log-lin makes it difficult to report information at the wall where $y^*=0$, it has been well revealed in other plots such as Fig.3.1 .The no slip case represented is in coherence with the results obtained by Kim et. al [15]. It is clearly visible that the y_{max}^* of the no slip case is higher than that of the slip case proving the reduction of friction Reynolds number of the slip case with a $Re_\tau \approx 152$. The drag reduction effect can be seen in the form of higher shift in the profile due to the introduction of velocity at the wall [22]. Note: The profiles are parallel and does not show the reduction of mean velocity of slip case close to centerline because of the $*$ units adopted. If the same profile is plotted in $+$ units, the effects of profile intersection would be visible well in advance as in Fig.3.4.

The effect of non-zero slip velocity is described better in Fig.3.3, where the mean slip velocity has been deducted from the mean velocity. It is clearly seen that the both the profiles fall into one as the deduction of slip velocity indicates a regular channel flow with no slip boundary conditions. The minimal deviation of the profiles at high y^* signals the requirement to increase the sample size.

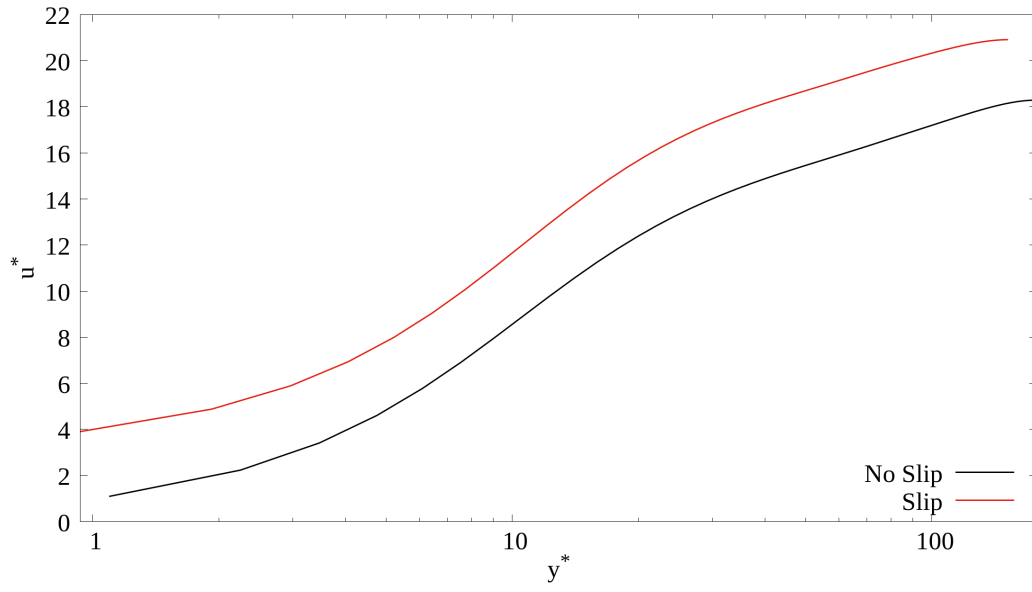


Figure 3.2: Mean streamwise velocity in * units

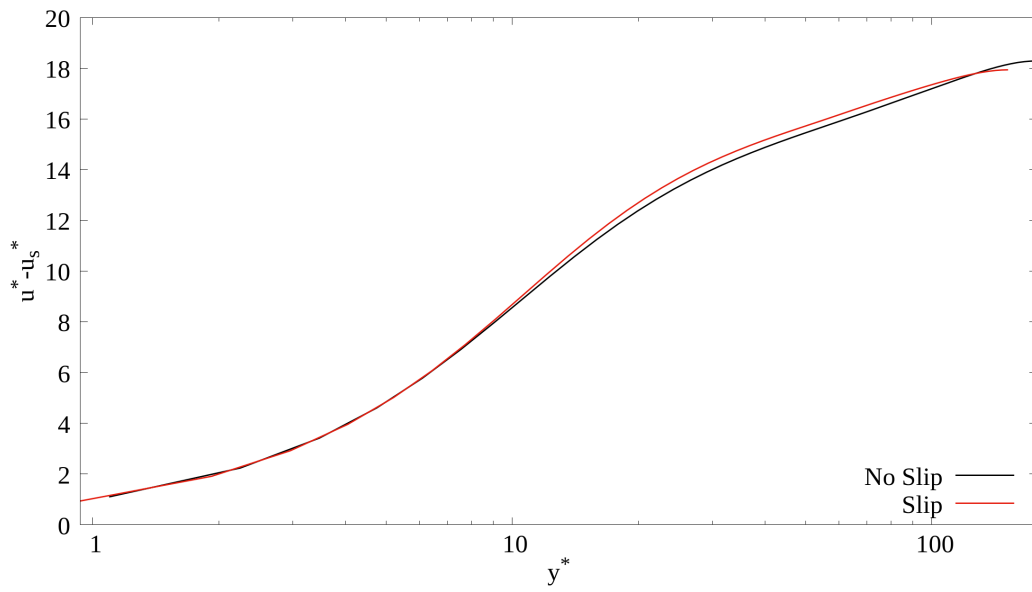


Figure 3.3: Mean velocity profile discarding slip velocity in * units

$$\begin{aligned}
 c_f &= \frac{\tau_w}{\frac{1}{2}\rho U_c^2} \\
 C_f &= \frac{\tau_w}{\frac{1}{2}\rho U_b^2}
 \end{aligned}
 \tag{3.6}$$

3.5. Law of the wall

When a turbulent flow over walls is analysed, there are two length scales that are taken under consideration. The viscous length scale to describe closer to the wall y/δ_ν or y^+ , and the geometric length scale y/δ when the analysis is closer to the centerline. The postulation of the law of the wall informs that velocity gradient $\frac{d\bar{u}}{dy}$ depends upon the aforementioned length scales through a universal non-dimensional function as expressed in eq.(3.7) [24].

$$\frac{d\bar{u}}{dy} = \frac{u_\tau}{y} \Phi\left(\frac{y}{\delta_\nu}, \frac{y}{\delta}\right) \quad (3.7)$$

where Φ is the universal non-dimensional function.

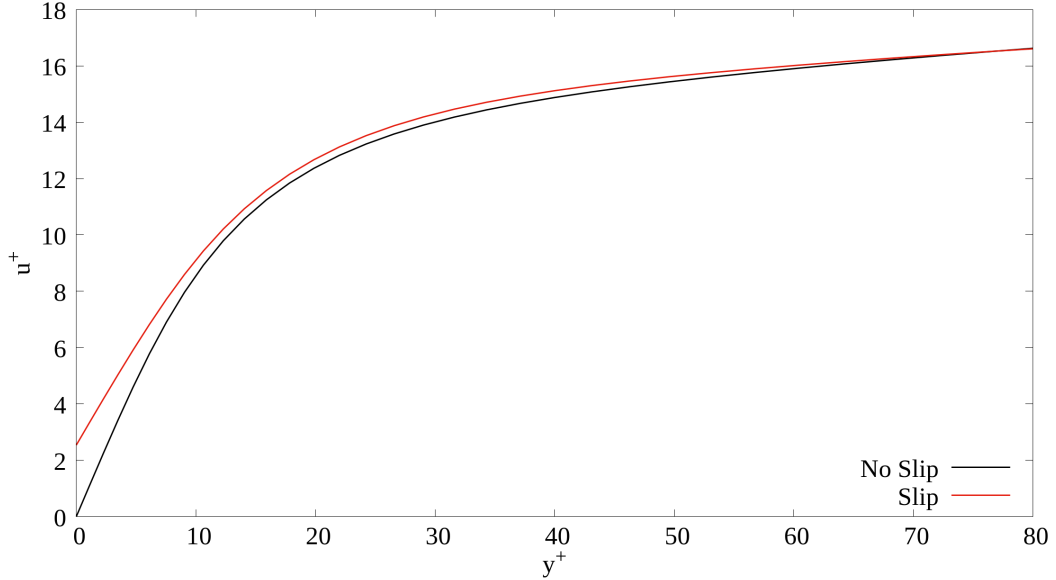


Figure 3.4: Mean velocity near wall in + units

In the inner region, there exists the viscous sublayer ($y^+ < 5$), where from the eq.(3.7), a relation can be expressed for u^+ in that region. At such low scales the viscous length scale dominates and the global length scale can be discarded from Φ . After applying this hypothesis, if the equation is integrated and no slip boundary conditions are applied, it can be seen that in the viscous sublayer, the u^+ is solely dependent on y^+ and this dependency is linear. Essentially, when $y^+ \approx 5$, the value of u^+ is roughly the same of y^+ . In Fig.3.4, the mean profile in + units are plotted against y^+ closer to the wall until $y^+ = 80$ to show the mentioned effects. It can be clearly seen in the figure, that when looked extremely closer to the wall $y^+ < 5$, the law of the wall holds, where the values of u^+ is roughly equal to that of y^+ for the no-slip case. When transitioned to the slip case, the

law does not hold due to the introduction of slip velocity which violates the assumptions involved in the postulation of the law.

The another region of interest is the so called 'log-law region' which in the non-dimensional scale is when $y^+ > 30$. In this region, the viscous significance already gets weaker and therefore in the function Φ , the dependence of viscous length scales can be dropped. This results into the case where Φ adopts a constant value thereby resulting in the log-law expressed in eq.(3.8) [24].

$$u^+ = \kappa^{-1} \ln(y^+) + B \quad (3.8)$$

where κ is the Von Karman constant and B an additive constant.

When observed the Fig.3.4, it is clear that both the cases exhibit a log-law behaviour. It can be also be observed that when plotted in $+$ units, in the region where the log-law holds, the agreement between the cases seem to get better as the viscous dominance is now lost. The same effect is not true for $*$ scaling as seen in Fig.3.2. The Fig.3.2 confirms the vertical shift of ΔB (where Δ denotes differences between slip and no slip case) from the eq.(3.8). In other words, it can be said that a positive change in ΔB can be seen as an amount of drag reduction [17]. From a physical standpoint, this upward shift of the log layer can be thought of as broadening of the viscous sub layer [6].

3.5.1. ΔB : A theoretical comparison

Gatti & Quadrio [11] derived a relation between ΔB and the drag reduction rate R_d starting from the velocity-defect law. In the region farther away from the wall, the velocity-defect law describes the differences in local mean velocity and centerline mean velocity as reported in eq.(3.9) [24].

$$u_c^+ - \bar{u}^+ = -\frac{1}{\kappa} \ln\left(\frac{y}{\delta}\right) + B_1 \quad (3.9)$$

where B_1 is a flow dependent constant.

When eqn.(3.8) and (3.9) are added together and u_c is transformed to u_b through the relation $u_c^+ = u_b^+ + \kappa^{-1}$ [24], it takes the form of the friction law which relates C_f and Re_τ . It was shown in [11] that when this friction law written for the controlled case is subtracted from the the reference case, two equations are derived relating ΔB and R_d : One for CPG case and the other for CFR case. Since in this study, CFR approach is followed, the

equation for constant flow rate comparison is taken and reported here in eq.(3.10)

$$\Delta B = \sqrt{\frac{2}{C_{f_0}}}[(1 - R_d)^{-\frac{1}{2}} - 1] - \frac{1}{2\kappa} \ln(1 - R_d) \quad (3.10)$$

where C_{f_0} is the skin friction coefficient of the no slip case.

From the fig.3.2, ΔB was computed between the slip and the no slip case and it was compared with the value obtained from eq.(3.10). The values of R_d were computed from eq.(3.3) which were equal to a value of 0.26. When further substituted in the eq.(3.10), the value of ΔB came to be 2.99. On the other hand, when ΔB was directly computed from the DNS data, it was equal to a value of 3.02. It is evident that there is an excellent agreement between the DNS data and the theoretical prediction. As explained in previous passages that a positive ΔB is a sign of drag reduction, this agreement further supports the argument presented so far about the slip case.

3.6. Turbulent Intensities

As mentioned in Sec.3.3, this section is dedicated to understand the statistics of fluctuations. These fluctuations or turbulent intensities are commonly represented with the parameter root mean square (rms) of fluctuating velocity component as in eq.(3.11).

$$u_{rms} = \sqrt{u'^2} \quad (3.11)$$

In Fig.3.5, the rms of fluctuating velocities in * units have been plotted. As expected, the streamwise intensities peak compared to the other components with wall normal intensity v_{rms} being the least. The plot clearly shows that in a turbulent channel flow, anisotropy exists upto the centerline. It is further evident from the Fig.3.5, that the turbulent intensities peak near the wall in the viscous wall region $y/\delta < 0.2$ [24], signalling production activity due to the intense viscous dominance and relax as proceeded away from the wall where the viscous information is lost. Therefore the emphasis has to be given in the near wall region.

The behaviour of the no slip case is as expected and verified with the paper of Kim et. al [15] for $Re_\tau=180$. When plotted this way, it can be seen that the u_{rms} of slip case is infact higher than that of the no slip case. It can also be seen that the spanwise and wall normal intensities of the no slip case are now closer to that of the slip case. These effects indicate a reduction in drag, as the scaling has been adjusted with the corresponding

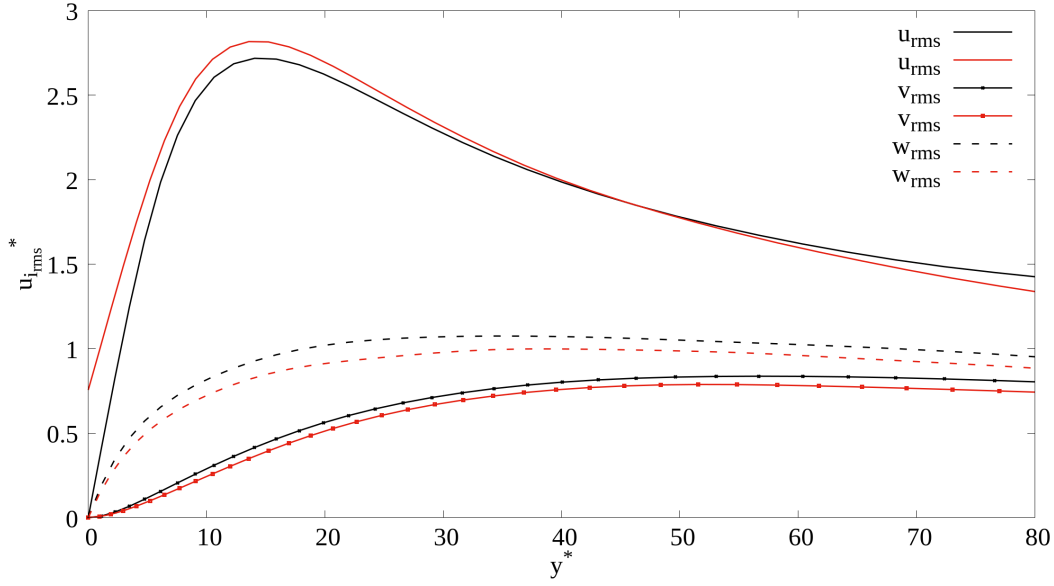


Figure 3.5: Turbulent intensities u_{rms}^* vs y^*

friction velocities. The increase in rms components in the slip case with this scaling is a direct consequence of the reduced friction velocity of the same case.

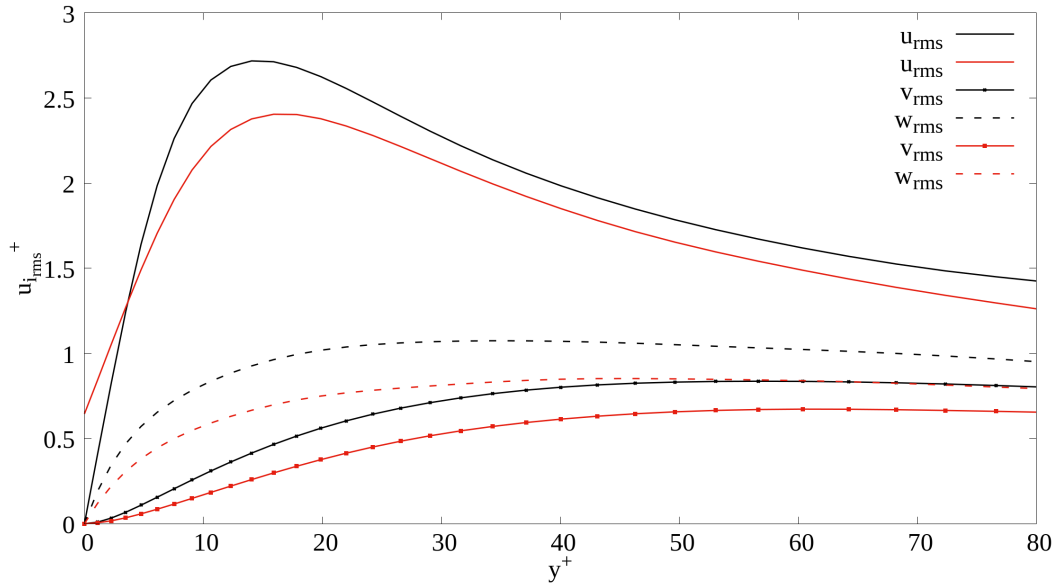


Figure 3.6: Turbulent intensities: u_{rms}^+ vs y^+

In order to examine the differences in turbulence activity of the two cases in the near wall region, the plot has been rescaled in $+$ units in Fig.3.6. It is important to observe that the peak of rms quantities near wall have been significantly reduced with the slip case informing the reduction of vigorous turbulent activity, which is coherent with the

observation of Min&Kim [22]. Despite this, the increase of u_{rms} (peak value $u_{rms} \approx 2.3u_{\tau_0}$) near the wall can be attributed to the fluctuation of slip velocity u_s [22]. It is also clear how this scaling with the friction velocity u_{τ_0} can be highly representative of the velocity fluctuations, Eg: u_{rms} is 270% of u_{τ_0} at the peak for no slip case and is 230% of u_{τ_0} in slip case which is a clear indication of reduction of production activity.

3.7. Shear Stresses

Having characterized the statistics of mean and turbulent properties, the next step in the analysis of the boundary conditions is quantifying the stresses. The total stress in a turbulent flow consists of two components. The viscous stress and the Reynolds shear stress as reported in eq.(3.12). The first component is the conventional definition of shear stress also called as Laminar shear stress whereas the second component namely the Reynolds shear stress is a peculiar property of turbulent flows.

$$\tau = \mu \frac{d\bar{u}}{dy} - \rho \overline{u'v'} \quad (3.12)$$

where τ is the shear stress μ the dynamic viscosity of the fluid, \bar{u} the mean velocity and u' the fluctuating streamwise velocity component.

In Fig.3.7, the stress profiles individually have been shown against the wall normal distance. Fig.3.7a demonstrates how viscous stress behaves across the half-channel. The viscous shear stress in this plot have been normalised with respect to the total shear stress at the wall. The behaviour is expected such that viscous stress coming from the first term of eq.(3.12) is a highly near wall phenomenon and quickly drops as soon as the information of viscosity is lost at $y/\delta \approx 0.2$. As the Reynolds number increases, this effect is more pronounced [24]. Hence, it can be seen from the same plot where the slip case is shifted to the right describing low Reynolds number effects.

Since the viscous and Reynolds stresses summed up together is the total stress, these two are complementary in nature. This effect is visible at $y/\delta \approx 0.2$ in Fig.3.7b where the Reynolds stress normalised with total stress in * units peak exactly where the shear stress dips. The same low Reynolds number effect is also visible here where the Reynolds shear stress increases at a higher wall normal distance compared to the no slip case. The no slip condition in the no slip case and no penetration condition in slip case make the Reynolds stress go to zero at the wall. As the centerline is approached, the shear stress and mean velocity gradient vanishes making the normalised stresses go to zero [24]

This description can be visualised better in Fig.3.8 where the same quantities but now

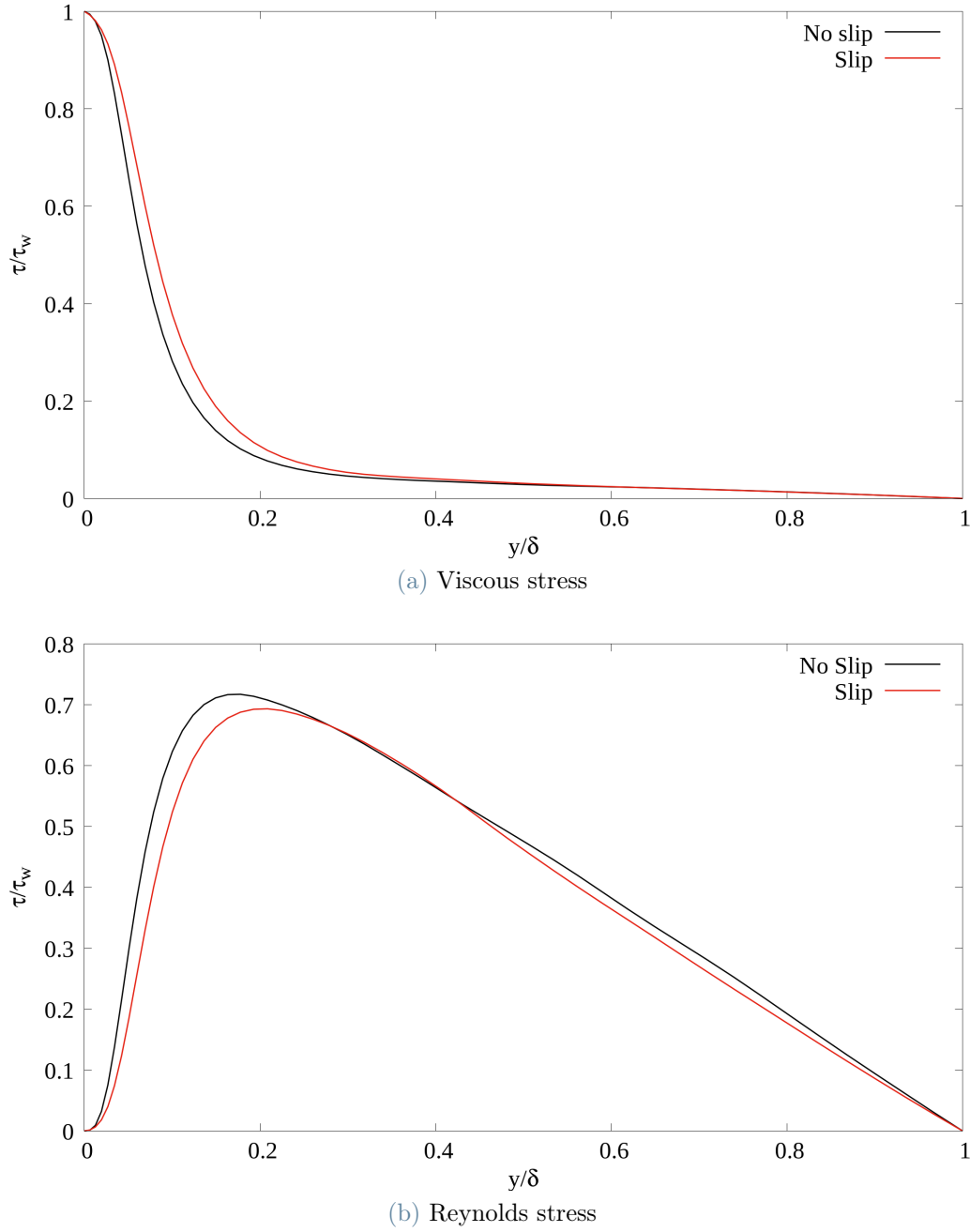


Figure 3.7: Stress profiles in $*$ units

combined have been plotted against y^* upto the value of sixty to magnify the effect of near wall region. Although a discrepancy is spotted in Reynolds stress in the same figure where it is expected to be a straight line in the region $y^* \approx 40 - 60$, whereas a wavery nature is visible in the figure. This can be attributed to the inadequacy of sampling while gathering statistics.

The eq.(3.12) can also take another form as given in eq.(3.13). It is clear from the

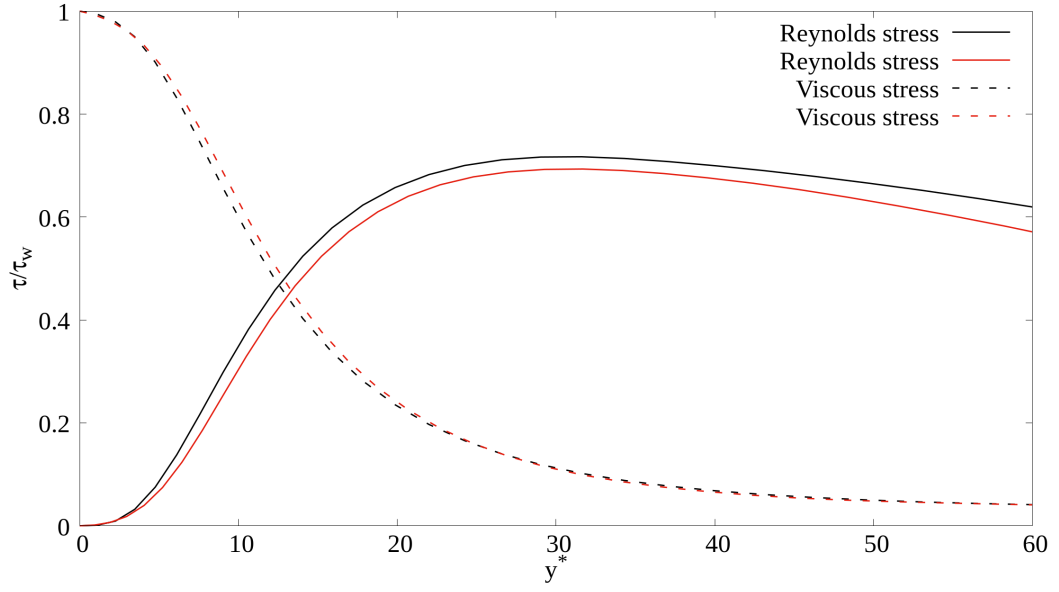


Figure 3.8: Combination of Viscous and Reynolds Stress

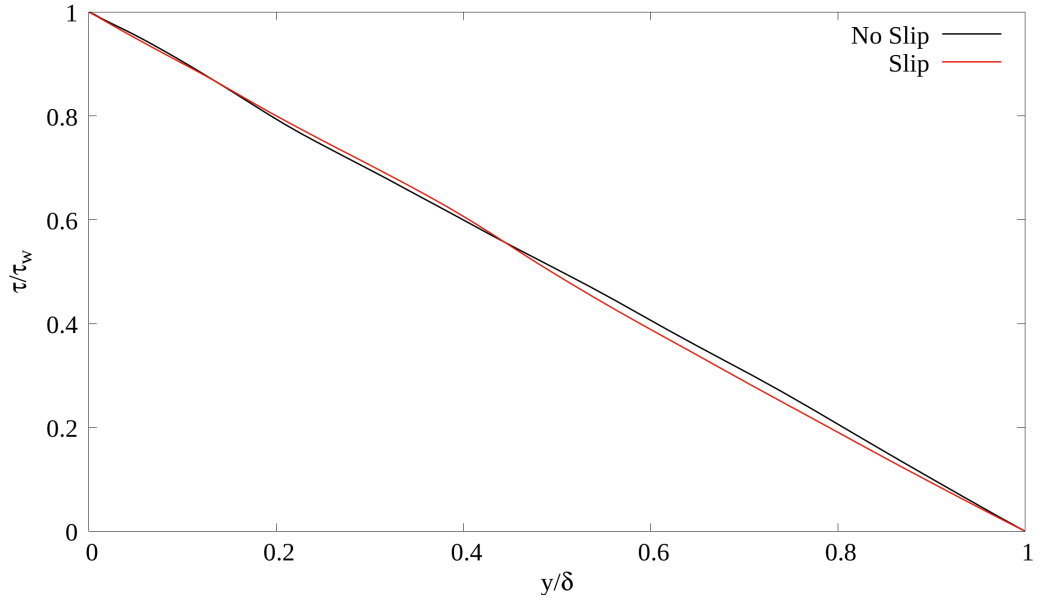
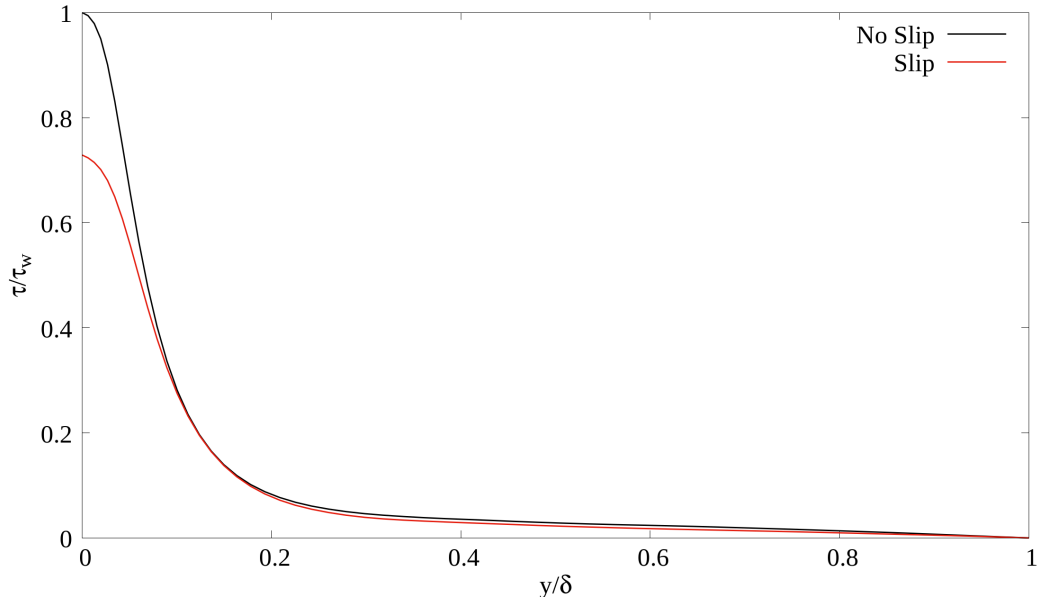
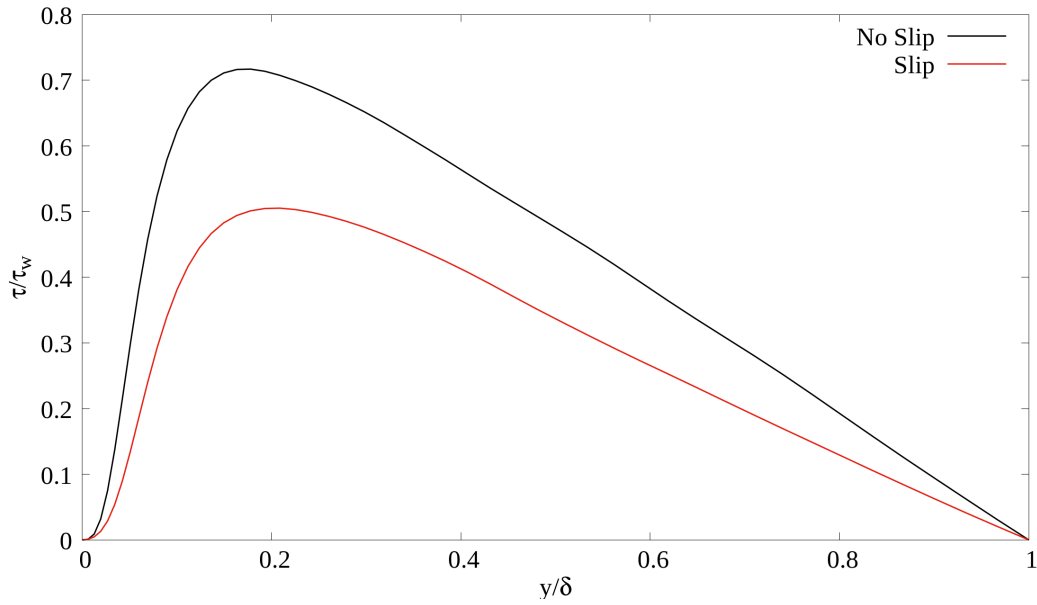


Figure 3.9: Total stress

equation that the total stress when normalised with the total shear stress at the wall has a linear relation with the wall normal distance. This linearity is clearly visible when the normalised shear stress is plotted in * units in Fig.3.9. As the plot is in * units and thereby normalised with actual shear stress at the wall, both the slip and no slip lines should coincide. Although this coincidence is visible, some discrepancies are also spotted where the profiles deviate from each other. These deviations indicate again the inadequacy in sampling.



(a) Viscous stress



(b) Reynolds stress

Figure 3.10: Stress profiles in + units

$$\tau(y) = \tau_w \left(1 - \frac{y}{\delta}\right) \quad (3.13)$$

As the general nature is well understood and verified, to characterize the differences in statistics that occur in slip case, the same plots are now plotted in + units in Fig.3.10 for a better comparison.

When the statistics are re-scaled in this way where the stresses are now normalised with the shear stress at the wall of no slip case, some deviations are clearly visible with respect to the no slip case. The important differences arise very close to the wall, where the slip velocity has a greater impact on the shear stress at the wall reducing both Reynolds and viscous stresses. It can be seen in Fig.3.10a, that the numerical value of $\tau/\tau_w \approx 0.73$ for the slip case. Since the Reynolds stresses are null at the wall, this essentially implies that the total shear stress at the wall in slip case is 73% of the total shear stress with a no-slip wall. This is in well agreement with the data presented in Sec.3.1 in table 3.1 where it reports a 27% drag reduction in slip case. It can also be seen in Fig.3.10b, that the peak of the Reynolds stresses are significantly trimmed by 27% in the slip case with respect to the no slip case.

3.8. Turbulent Kinetic Energy

To describe the energy associated with the eddies in a turbulent flow, the quantifiable parameter is the turbulent kinetic energy which by definition is the mean kinetic energy per unit mass associated with the eddies. The symmetric Reynolds stress tensor consists of four non-zero components $u'u'$, $v'v'$, $w'w'$, $u'v'$. Turbulent kinetic energy henceforth denoted by TKE is the half of the trace of Reynolds stress tensor as given in eq.3.14

$$k = \frac{1}{2}(\overline{u'^2} + \overline{v'^2} + \overline{w'^2}) \quad (3.14)$$

where k is the turbulent kinetic energy and u' , v' , w' denote the streamwise, wall-normal and spanwise velocity fluctuations respectively.

The TKE in * units have been plotted in Fig.3.11. The behaviour is very evident in the plot that intensity is high near the wall due to the streamwise fluctuations and relax further as moved away from the wall. When plotted this way, it can be noticed that the TKE of slip case is infact higher than the no slip case. This is the effect of scaling with a similar reasoning to the one described about Fig.3.5.

The TKE normalised with shear scales in + units against y^+ has been reported in Fig.3.12. From the figure, there is no ambiguity at all with the fact that the introduction of slip velocity reduces the production of TKE near the wall as all the diagonal components of Reynolds stress tensor have reduced in magnitude. At the wall, the turbulent kinetic energy is zero for the no slip case from (3.14). Whereas in the slip case, the introduction of non zero slip velocity contributes to the TKE bringing the non-dimensionalised $k \approx 0.2$

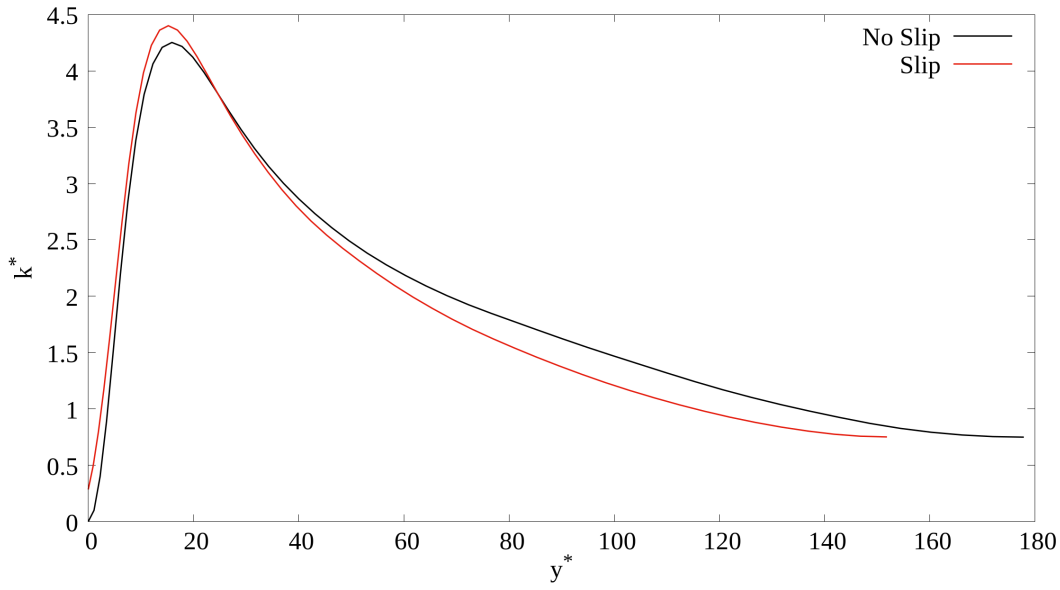


Figure 3.11: Turbulent Kinetic Energy in * units

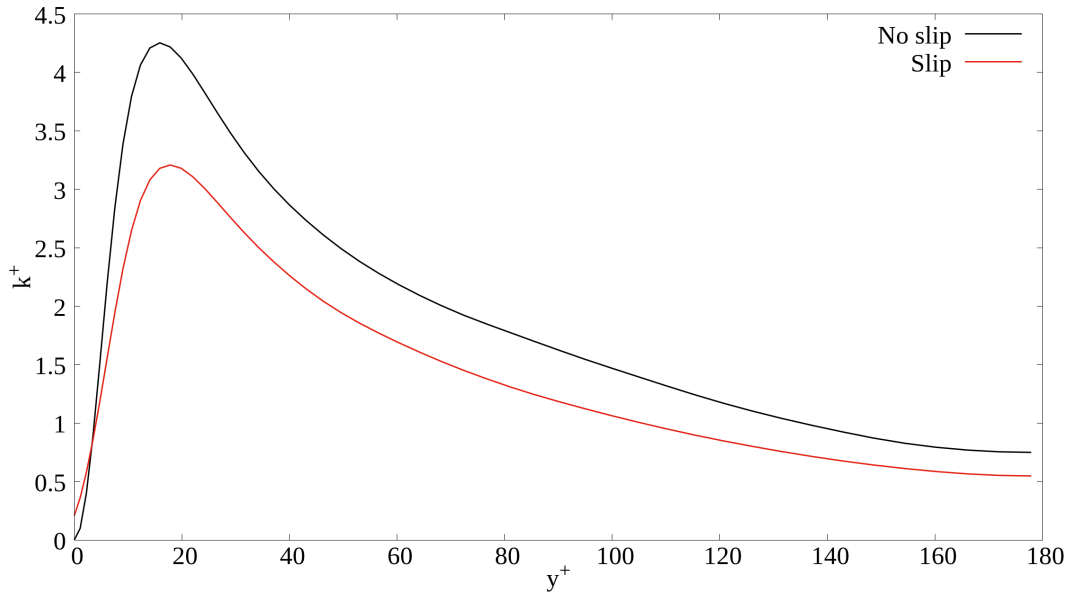


Figure 3.12: Turbulent Kinetic Energy in + units

The approximate self similarity in the log law region is also noticeable. To visualise this effect better and to highlight Reynolds stresses in a different perspective, it can be shown with the normalisation with TKE as shown in Fig.3.13 where the Reynolds stresses are approximately uniform in the log-law region. A peculiarity with such scaling is that this informs how the Reynolds stresses contribute to the TKE, as the sum of diagonal Reynolds stresses should be equal to twice the amount of TKE from the expression (3.14).

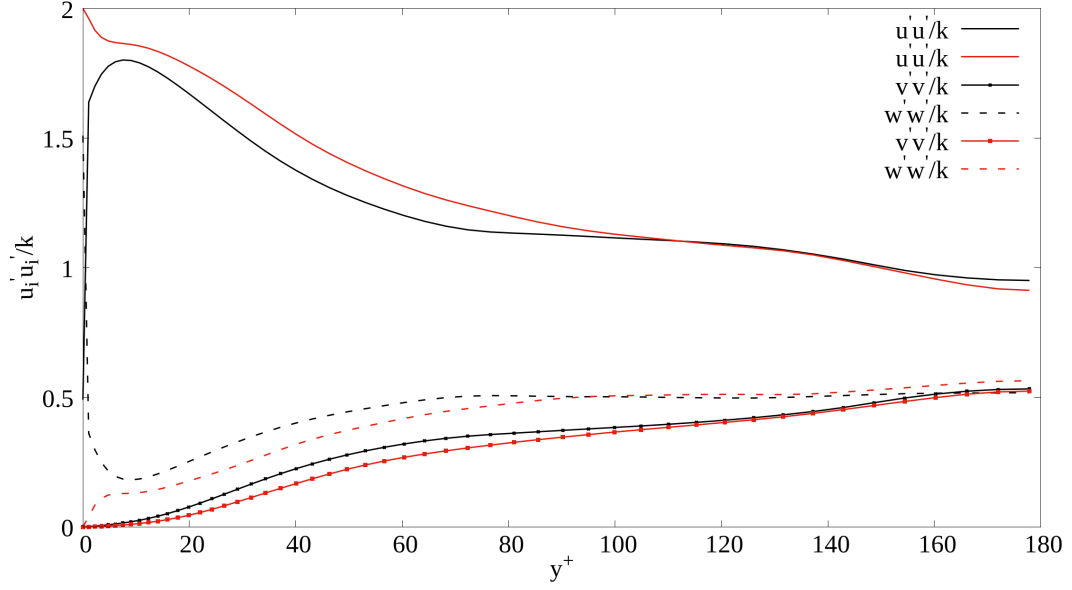


Figure 3.13: Reynolds stresses normalised by turbulent kinetic energy in + units

On the note of comparison between the cases, in the no-slip case, TKE goes to zero at the wall due to no-slip and no penetration conditions. Note: Although in the Fig:3.13, the values of no slip case at the wall are not zero for $u'u'$ and $w'w'$, it is merely due to the scaling introduced as the summation should be equal to a value of two as per eq.(3.14). They represent the contribution to the TKE and not directly the numerical values of components itself. On the other hand, with the slip case, the components $v'v'$ and $w'w'$ are null at the wall due to no slip and no penetration conditions. Therefore all the kinetic energy contribution at the wall comes from the slip velocity, which is represented by a numerical value of two with this scaling in Fig.3.13. It can be further seen that if the value of TKE at the wall from Fig.3.12 ($k/u_{\tau^2} \approx 0.2$) is substituted here, it results that $u'u'/u_{\tau_0}^2 \approx 0.4$ at the wall, which further implies that $u_{rms}^+ \approx 0.6$ which can be seen in Fig.3.6. Therefore, this scaling also provides a convenient navigation among different quantities. It is further interesting to note that at the centerline, roughly half of the kinetic energy contribution comes from $u'u'$ and the rest half is shared among $v'v'$ and $w'w'$. This is a direct consequence of the anisotropy extending upto centerline as observed in the properties of turbulent intensities.

So far, the statistics were analysed for TKE and its production, whereas in the Fig.3.14, the analysis is not restricted to production but also includes dissipation. When a budget equation for turbulent kinetic energy is written, it is balanced by two source terms namely

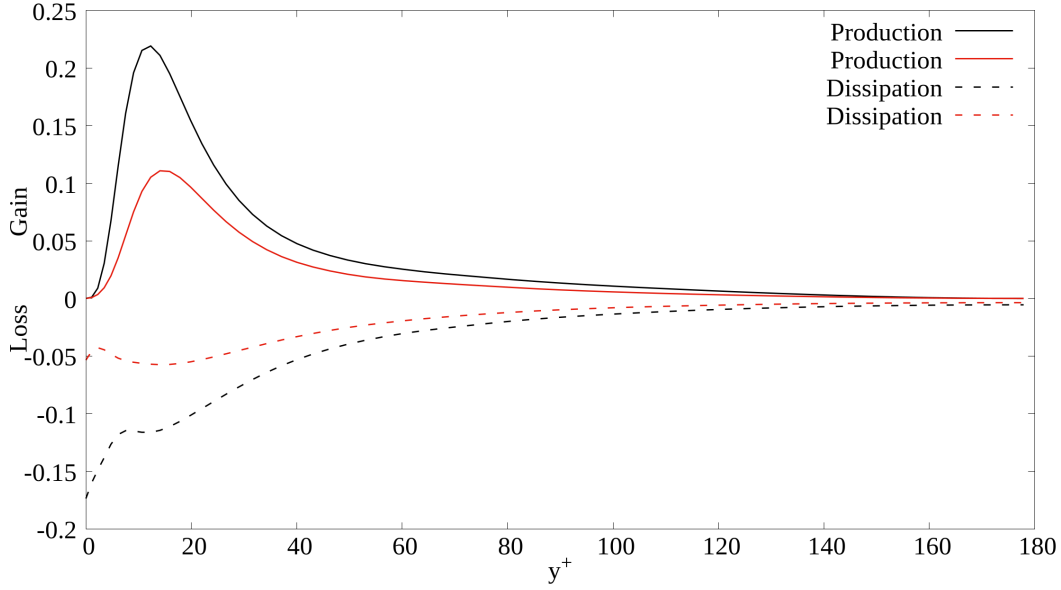


Figure 3.14: Production and Dissipation as gain and loss in + units

production and dissipation which are expressed as follows in eqs. (3.15) & (3.16).

$$P = -\overline{u_i' u_j'} \frac{\partial \overline{u_i}}{\partial x_j} \quad (3.15)$$

$$\epsilon = 2\nu \overline{s_{ij}' s_{ij}'} \quad (3.16)$$

where P denotes production and ϵ is dissipation.

In Fig.3.14, the production and dissipation terms normalised by friction units (+) are plotted against y^+ as a gain and loss figure. As shown in the previous plots, the production peaks in the buffer layer at $y^+ \approx 17$ for the no slip case. The production term is essentially made up of product of Reynolds stresses and viscous stresses from the terms seen, and since these two stresses exhibit complimentary behaviour, the peak production happens exactly at the wall normal distance when Reynolds shear stress and viscous stress are equal [24]. This effect can also be seen in slip case where now there is a slight shift of the peak in the wall normal direction. This shift can also be corroborated in Fig.3.8 which also shows a slight delay of the equal point of the two stresses.

The dissipation in general for a no slip case peaks at the wall, despite the turbulent kinetic energy being zero as it is balanced by only viscous transport term from the budget equation of k. In the slip case, the trends vary slightly as now the budget equation contains more non-zero terms and the dissipation therefore is not solely balanced by the

viscous transport. In consistence with whatever has been described in other sections, as the centerline is approached the viscous dominance is significantly reduced and therefore production and dissipation which depend upon it also reduces. Whereas, at the centreline the absence of mean velocity gradient and shear stress make the quantities null.

4 | Conclusions and Future developments

The turbulent flow over a channel with slip boundary conditions was analysed with an intention to understand how the imposed slip velocity imparts drag reduction and modifies the turbulence dynamics especially near the wall. The results from the simulations are then compared with the no slip reference cases that have been validated with Kim et.al [15]. The study is based on the idea that inclining a modulated partial slip system could lead to friction drag reduction by inducing spanwise forcing much like the active spanwise forcing methods [25] [14]. However, the lack of exposure and literature in the aforementioned idea forces one to perform this work to better understand the slip effects on turbulence and validating the employed methodology. The major result that arose out of the study is the percentage of drag reduction in comparison to the reference no slip case. The percentage was found to be in accordance with the results obtained by Min-Kim [22]. It was observed that imposing solely the streamwise slip velocity creates a lower resistance at the wall creating an offset in the mean streamwise velocity at the wall. This implies the shear stress at the wall where the whole contribution comes from the viscous stresses have reduced essentially reducing the skin-friction drag. Instead, when the turbulent intensities are looked, it shows that inducing solely the streamwise slip velocity at the wall lowers the production activity and all the rms components of velocities show a reduction in contrast with the reference case. These characteristics remain the same when stresses were analysed. It was evident that the shear stress at the wall have reduced significantly and the increase of Reynolds stresses near the wall has a delay signalling a delay in peak of the production activity farther away from the wall, from where dissipation acts quicker moving towards the centerline and thereby controlling the turbulence activity. Finally, the turbulent kinetic energy was studied as a consequence of slip velocity. As the production of turbulent kinetic energy depend upon the Reynolds and viscous stresses, the behaviour is predictable with the description of stresses. Hence, the turbulent kinetic energy is now not singular at the wall as it is in the no slip case, due to the presence of streamwise velocity. It is also worth mentioning that all of the contribution to the turbulent kinetic energy at

the wall comes from the streamwise fluctuating velocity which when non dimensionalised is exactly the twice of turbulent kinetic energy. As proceeded away from the wall, the spanwise and wall normal components start contributing to the turbulent kinetic energy, yet the streamwise component maintaining the highest contribution.

The work clearly indicates that the streamwise slip has significant effects on the behaviour of turbulent flow. Although the results are in preliminary sense and not meant for quantitative reproduction, it clearly validates the performance of the code and indicates that the code is ready to perform the partial slip and spanwise forcing. In order to proceed further, the problems arise despite this validation performed in this study due to lack of literature. Therefore, various cautionary steps have to be taken along the way. Since the final case of partial slip involves slip in both streamwise and spanwise directions, a possible approach could be to study the case of spanwise slip and their drag increasing property as concluded by Min-Kim [22]. Then inhomogeneity in the boundary conditions could be introduced by streamwise slip along the channel but only for half the spanwise length, the rest half being a no slip boundary condition. Although this case cannot be verified in literature, an intuitive result in drag reduction should be nearly half of the number obtained in this study. The statistics have to be captured appropriately and if they turn in favour, the only step left is to perform the primary objective and possibly achieve drag reduction.

Bibliography

- [1] BECHERT, D., AND BARTENWERFER, M. The viscous flow on surfaces with longitudinal ribs. *Journal of Fluid Mechanics* 206 (1989), 105–209.
- [2] BUSSE, A., AND SANDHAM, N. Influence of an anisotropic slip-length boundary condition on turbulent channel flow. *Physics of Fluids* 24, 5 (2012).
- [3] CHECCO, A., OCKO, B. M., RAHMAN, A., BLACK, C. T., TASINKEVYCH, M., GIACOMELLO, A., AND DIETRICH, S. Collapse and reversibility of the superhydrophobic state on nanotextured surfaces. *Phys. Rev. Lett.* 112 (May 2014), 216101.
- [4] CHOI, C.-H., WESTIN, K. J. A., AND BREUER, K. S. Apparent slip flows in hydrophilic and hydrophobic microchannels. *Physics of Fluids* 15, 10 (09 2003), 2897–2902.
- [5] CHOI, H., MOIN, P., AND KIM, J. Direct numerical simulation of turbulent flow over riblets. *J Fluid Mechanics* 255 (Oct. 1993), 503–539.
- [6] CHOI, K.-S. Near-wall structure of a turbulent boundary layer with riblets. *Journal of Fluid Mechanics* 208 (1989), 417–458.
- [7] DEAN, R. Reynolds number dependence of skin friction and other bulk flow variables in two-dimensional rectangular duct flow. *Trans. ASME I: J. Fluids Eng.* 100 (1978), 215–223.
- [8] FUKAGATA, K., KASAGI, N., AND KOUMOUTSAKOS, P. A theoretical prediction of friction drag reduction in turbulent flow by superhydrophobic surfaces. *Physics of Fluids* 18, 5 (05 2006), 051703.
- [9] GARCÍA-MAYORAL, R., AND JIMÉNEZ, J. Drag reduction by riblets. *Philos. Trans. A Math. Phys. Eng. Sci.* 369, 1940 (Apr. 2011), 1412–1427.
- [10] GARCIA-MAYORAL, R., AND JIMÉNEZ, J. Hydrodynamic stability and the breakdown of the viscous regime over riblets. *J. Fluid. Mech.* 678 (2011), 317–347.

- [11] GATTI, D., AND QUADRIO, M. Reynolds-number dependence of turbulent skin-friction drag reduction induced by spanwise forcing. *J. Fluid Mech.* 802 (2016), 553–58.
- [12] GHEBALI, S., CHERNYSHENKO, S., AND LESCHZINER, M. Can large-scale oblique undulations on a solid wall reduce the turbulent drag? *Physics of Fluids* 29, 10 (Oct. 2017), 105102.
- [13] HASEGAWA, Y., FROHNAPFEL, B., AND KASAGI, N. Effects of spatially varying slip length on friction drag reduction in wall turbulence. *Journal of Physics: Conference Series* 318, 2 (Dec. 2011), 022028.
- [14] JUNG, W., MANGIAVACCHI, N., AND AKHAVAN, R. Suppression of turbulence in wall-bounded flows by high-frequency spanwise oscillations. *Phys. Fluids A* 4 (8) (1992), 1605–1607.
- [15] KIM, J., MOIN, P., AND MOSER, R. Turbulence statistics in fully developed channel flow at low Reynolds number. *Journal of Fluid Mechanics* 177 (1987), 133–166.
- [16] LELE, S. K. Compact finite difference schemes with spectral-like resolution. *Journal of Computational Physics* 103, 1 (1992), 16–42.
- [17] LUCHINI, P. Reducing the turbulent skin friction. In *Computational Methods in Applied Sciences 1996*, Desideri et al., Ed. Wiley, 1996.
- [18] LUCHINI, P. CPL. Available at <https://CPLcode.net>, 2020.
- [19] LUCHINI, P., MANZO, F., AND POZZI, A. Resistance of a grooved surface to parallel flow and cross-flow. *Journal of Fluid Mechanics* 228 (1991), 87–109.
- [20] LUCHINI, P., AND QUADRIO, M. A low-cost parallel implementation of direct numerical simulation of wall turbulence. *J. Comp. Phys.* 211, 2 (2006), 551–571.
- [21] MARTELL, M. B., PEROT, J. B., AND ROTHSTEIN, J. P. Direct numerical simulations of turbulent flows over superhydrophobic surfaces. *Journal of Fluid Mechanics* 620 (2009), 31–41.
- [22] MIN, T., AND KIM, J. Effects of hydrophobic surface on skin-friction drag. *Physics of Fluids* 16, 7 (05 2004), L55–L58.
- [23] PIT, R., HERVET, H., AND LILIANE, L. Direct experimental evidence of slip in hexadecane: Solid interfaces. *Physical review letters* 85 (08 2000), 980–3.
- [24] POPE, S. *Turbulent Flows*. Cambridge University Press, Cambridge, 2000.

- [25] QUADRIO, M., RICCO, P., AND VIOTTI, C. Streamwise-traveling waves of spanwise wall velocity for turbulent drag reduction. *J. Fluid Mech.* 627 (2009), 161–178.
- [26] RASTEGARI, A., AND AKHAVAN, R. The common mechanism of turbulent skin-friction drag reduction with superhydrophobic longitudinal microgrooves and riblets. *Journal of Fluid Mechanics* 838 (Mar. 2018), 68–104. Publisher: Cambridge University Press.
- [27] ROTHSTEIN, J. P. Slip on superhydrophobic surfaces. *Annual Review of Fluid Mechanics* 42, 1 (2010), 89–109.
- [28] WALSH, M. *Turbulent boundary layer drag reduction using riblets.*
- [29] WALSH, M. Drag characteristics of v-groove and transverse curvature riblets. *In Viscous Drag reduction (ed. G.R. Hough). American Institute of Aeronautics and Astronautics.* (1980).

List of Figures

1.1	Sketch of a channel wall with alternating boundary conditions and inclined by an angle θ with respect to the streamwise direction [13]. x and z denote streamwise and spanwise directions respectively	2
2.1	Computational domain [20]	6
3.1	Mean Profile over channel half height in global units; \bar{u} :Mean Velocity . . .	19
3.2	Mean streamwise velocity in * units	20
3.3	Mean velocity profile discarding slip velocity in * units	20
3.4	Mean velocity near wall in + units	21
3.5	Turbulent intensities u_{rms}^* vs y^*	24
3.6	Turbulent intensities: u_{rms}^+ vs y^+	24
3.7	Stress profiles in * units	26
3.8	Combination of Viscous and Reynolds Stress	27
3.9	Total stress	27
3.10	Stress profiles in + units	28
3.11	Turbulent Kinetic Energy in * units	30
3.12	Turbulent Kinetic Energy in + units	30
3.13	Reynolds stresses normalised by turbulent kinetic energy in + units	31
3.14	Production and Dissipation as gain and loss in + units	32

Acknowledgements

This work is incomplete if the contributions of others involved are not recognised. I am sincerely grateful to Prof. Maurizio Quadrio for providing immense guidance throughout the period and for his constant presence. I am also thankful to Nil Couto for sharing and discussing ideas that helped me a lot in the process.

Abstract in Italian

Un flusso turbolento in un canale è analizzato con l'obiettivo principale di ridurre la resistenza al taglio della pelle mediante la modulazione spaziale dello scivolamento parziale. Ci si aspetta che questa modulazione spaziale produca forze spanwise e sopprima la turbolenza in modo simile alle tecniche di controllo attivo, come le tecniche di parete oscillante e le onde viaggianti. Una tale strategia supera gli inconvenienti energetici del controllo attivo. Tuttavia, la mancanza di esposizione in tali casi di scivolamento parziale richiede di approfondire casi con una letteratura abbondante che possa fare luce sul fenomeno di riduzione della resistenza. Lo studio mira a farlo utilizzando le condizioni di scivolamento. Per simulare il flusso, sono stati impiegati Simulazioni Numeriche Dirette (DNS) con un approccio pseudospettrale. Le simulazioni sono state condotte con dati simili alla letteratura pertinente per un confronto accurato. Inoltre, i casi di scivolamento sono confrontati con il controparte senza scivolamento per quantificare la riduzione della resistenza e caratterizzare le statistiche. Per garantire l'accuratezza, i casi di riferimento senza scivolamento sono convalidati con la letteratura pertinente. Si osserva che la presenza di condizioni di scivolamento lungo la direzione del flusso crea effetti a basso numero di Reynolds e riduce la resistenza al taglio della pelle. La riduzione della resistenza al taglio è corroborata da una procedura a due fasi. Inoltre, si osserva che l'introduzione della velocità di scivolamento modifica la dinamica della turbolenza, in particolare abbassando l'attività di produzione vicino alla parete. Sebbene il comportamento generale delle statistiche sia coerente con la conoscenza del flusso turbolento in canale, alcune tendenze specifiche devianti segnalano la necessità di aumentare la dimensione del campione. Alcune intuizioni sono fornite sulla modifica ulteriore della geometria per ottenere forze spanwise e possibilmente una riduzione della resistenza.

Keywords: scivolamento parziale, turbolenza, riduzione della resistenza, pseudo-spettrale